Applied Catalysis B: Environmental 165 (2015) 176–184

Contents lists available at ScienceDirect

Applied Catalysis B: Environmental

journal homepage: www.elsevier.com/locate/apcatb

Electro-oxidation of ethanol on ternary Pt–Sn–Ce/C catalysts

Juliana M. Jacob[a], Patricia G. Corradini[a], Ermete Antolini[b,*], Nathalia Abe Santos[a], Joelma Perez[a]

[a] Instituto de Química de São Carlos, USP, C. P. 780, São Carlos, SP 13560-970, Brazil
[b] Scuola di Scienza dei Materiali, Via 25 aprile 22, 16016 Cogoleto, Genova, Italy

ARTICLE INFO

Article history:
Received 15 July 2014
Received in revised form
29 September 2014
Accepted 3 October 2014
Available online 12 October 2014

Keywords:
Ternary catalysts
Pt–Sn–Ce/C
Fuel cell
Ethanol oxidation

ABSTRACT

Ternary Pt–Sn–Ce/C catalysts were prepared by a modified formic acid method, and their activity for the ethanol oxidation reaction (EOR) was compared to that of Pt–Sn/C, Pt–Ce/C and Pt/C catalysts. No bulk alloy formation was detected by XRD analysis. XPS measurements indicated no segregation on the catalyst surface and the presence of Sn(0) and SnO_x, Ce_2O_3 and CeO_2 oxides. The onset potential for CH_3CH_2OH oxidation on Pt–Sn/C and Pt–Sn–Ce/C (60:20:20) catalysts, which have the highest Sn content on the surface, was lower than that of Pt–Sn–Ce/C (70:20:10) and (50:20:30), Pt–Ce/C and Pt/C catalysts. This work highlights the dependence on the potential of the effect of cerium in Pt–Sn–Ce/C catalysts on the EOR activity and on the reaction mechanism. By derivative voltammograms, different reaction pathways at different potentials, involving Sn (at *ca.* 0.44 V *vs.* RHE), Sn + Ce (at *ca.* 0.55 V *vs.* RHE) and Ce (at *ca.* 0.67 V *vs.* RHE) were inferred. The Pt–Sn–Ce/C catalysts were less tolerant to poisoning by ethanol oxidation intermediate species than Pt/C and Pt–Sn/C, but more stable than Pt–Ce/C catalysts. DEFC tests at 90 °C indicated that a higher Sn surface content is more effective for ethanol oxidation than the addition of Ce to Pt–Sn/C.

1. Introduction

In view of a possible use as anode materials in direct ethanol fuel cells (DEFCs), the electro-catalytic activity for the ethanol oxidation reaction (EOR) in acid medium of Pt-based catalysts has been widely investigated [1–9]. Among various Pt-based binary catalysts, Pt–Sn has been reported as the most effective for the electro-oxidation of ethanol [5,6]. The addition of tin to platinum not only increases the activity of the catalyst towards the oxidation of ethanol and, as a consequence, the DEFC performance, but also changes the product distribution, improving the ethanol oxidation to acetaldehyde and acetic acid [10]. In both alloyed and non-alloyed catalysts Sn provides OH species to oxidize adsorbed residues, and enhances the formation of acetaldehyde and acetic acid. To further increase its EOR activity and stability and to promote C—C bond cleavage the addition of a third metal, in particular Ru [11], Ni [12–14] and Rh [12,13,15–18], to Pt–Sn has been investigated. Recently, the addition of rare earth metals to platinum-based catalysts for low-temperature fuel cells has been reported [19]. Among rare earths, the use of cerium in low-temperature fuel cells was mostly investigated. Cerium oxide, CeO_2, is one of the most widely used rare earth metal oxide as a promoter for metallic catalysts such as Pt. CeO_2 is a fluorite-structured oxide with high oxygen storage capacity associated with its rich oxygen vacancies and low redox potential between Ce^{3+} and Ce^{4+}. CeO_2 is regarded as a kind of oxygen tank to adjust oxygen concentration at the catalyst surface under reaction condition and it has the ability to act as an oxygen buffer [20]. Many studies have been addressed to the effect of the addition of CeO_2 to Pt-based binary and ternary catalysts on the electrochemical oxidation of low molecular weight alcohols [19]. More recently, a sphere-like monodispersed Ni-doped CeO_2 (Ni-CeO_2) nanoparticles prepared by a facile thermal decomposition method was used to promote the catalytic properties of the Pt/C catalyst in DEFCs [21]. The effect of ceria on the electrocatalytic activity of an alloyed Pt–Sn/C (3:1) catalyst for the EOR was investigated, and the results indicated that the addition of Ce to Pt–Sn/C increases the EOR activity [22]. The dependence of the EOR activity of alloyed Pt–Sn–Ce/C catalysts on Ce content went through a maximum. In this work the effect of Ce addition on the EOR activity and stability of Pt–Sn–Ce/C catalysts was evaluated. Pt–Sn–Ce/C and, for comparison, Pt–Sn/C and Pt–Ce/C electrocatalysts were prepared by a modified formic acid method [23]. The as-prepared materials were characterized by X-ray diffraction (XRD), transmission electron microscopy (TEM) and X-ray photoelectron spectroscopy

* Corresponding author. Tel.: +39 010 918 2880; fax: +39 010 918 2368.
E-mail address: ermantol@libero.it (E. Antolini).

http://dx.doi.org/10.1016/j.apcatb.2014.10.012
0926-3373/

(XPS) and were tested for carbon monoxide and ethanol oxidation in acid medium by CO stripping, linear sweep voltammetry (LSV) and chronoamperometry (CA) measurements.

2. Experimental

2.1. Catalysts preparation

Pt–Sn/C, Pt–Ce/C and Pt–Sn–Ce/C catalysts were obtained by a modified formic acid procedure. The methodology was adding carbon Vulcan® in 0.5 mol L^{-1} of formic acid (Sigma Aldrich; 98.0%) on pH adjusted to 12.5 and heat the mixture at 80 °C in a reducing in carbon monoxide (CO) atmosphere. A solution of $H_2PtCl_6{\cdot}6H_2O$ (Alfa Aesar, 99.9%) and $CeCl_3$ (Sigma Aldrich, 56.81 wt% Ce) and $SnCl_2$ (Sigma Aldrich, 99.0%). The precursor solution was added in an interval of 15 min. After the addition, the time of reaction was 30 min. The supported catalysts thus formed were filtered, washed with ultra-pure water and dried at 80 °C for 2 h. Catalysts were prepared with a ratio of 20 wt% of metal on carbon. Three reasons metallic atomic Pt–Ce (Pt:Ce: 90:10; 70:30 and 50:50) and Pt–Sn–Ce (Pt:Sn:Ce: 70:20:10, 60:20:20 and 50:20:30) were synthesized. The nominal atomic composition of Pt–Sn/C was Pt:Sn = 75:25. The obtained material was filtered and dried in an oven at 80 °C for 2 h.

2.2. Catalysts characterization

The Pt–Sn/C, Pt–Ce/C and Pt–Sn–Ce/C catalysts were examined by X-ray diffraction (XRD) using a Rigaku, model Ultima IV diffractometer using Cu Kα radiation (0.15406 nm). The X-ray diffractograms were obtained with a scan rate of 1° min^{-1} for 2θ values between 10° and 100°. The transmission electronic microscopy study was done using a Philips CM 200 microscope operating at 200 kV. The samples for the TEM analysis were prepared by ultrasonically dispersing the catalyst powders in ethanol. A drop of the suspension was applied onto a carbon-coated copper grid and dried in air.

X-ray photoelectron spectroscopy (XPS) analysis was carried into the SXS beamline endstation at the LNLS (National Synchrotron Light Laboratory, Brazil). The XPS spectra were collected using the incident photon energy (E_{ph}) of 1840 eV, provided by the InSb (1 1 1) double crystal monochromator. The hemispherical electron analyzer (Specs – Phoibos 150) was set to pass energy of 20 eV with 0.2 eV step energy and 200 ms/point acquisition time. The overall energy resolution achieved was about 0.2 eV at E_{ph} = 1840 eV. The base pressure of the analysis chamber was 1.3×10^{-9} mbar. The monochromator photon energy calibration was done at the Si K-edge (1839 eV). An additional calibration of the analyzer energy was performed using a standard Au foil (Au 4*f*). All XPS measurements were performed at room temperature, using a 45° takeoff angle. The inelastic background of the Pt 4*f*, Sn 3*d* and Ce 3*d* electron core-level spectra was subtracted by using Shirley's method. The composition of the surface layer was determined from the ratio of the relative peak areas corrected by sensitivity factors of the corresponding elements. The spectra were fitted without placing constraints using mixed Gaussian–Lorentzian profiles to Pt and Sn, and Doniach-Sunjic to Ce, with Gaussian–Lorentzian profiles. The width at half maximum (FWHM) varied between 1.6 and 2.0 eV and the accuracy of the peak positions was ±0.2 eV. The Doniach-Sunjic α factor was 0.003. Splitting parameter was maintained constant to Sn (8.5 ± 0.5 eV) and for Ce (18.1 ± 0.5 eV), according the literature [24,25].

2.3. Electrochemical measurements

All electrochemical measurements were done in a conventional electrochemical cell, with a Pt wire counter-electrode and a reversible hydrogen reference electrode (RHE). The Pt–Ce/C; Pt–Sn/C and Pt–Sn–Ce/C electrocatalysts were used as ultra-thin layers on a glassy carbon disk electrode (0.385 cm^2) previously polished down to alumina. In all cases, the catalysts layers had a metal (Pt + Sn + Ce) load of 28 μg cm^{-2}. The general electrochemical behavior was characterized by cyclic voltammetry in 0.5 mol L^{-1} H_2SO_4, and the electrocatalytic activity towards ethanol oxidation was evaluated in 0.5 mol L^{-1} ethanol acid solution by linear sweep voltammetry (LSV) and chronoamperometry. All experiments were done at 25 °C in Ar saturated solutions. CO stripping experiments were carried out in the following way: after recording a cyclic voltammetry curve in an Ar purged system, CO was admitted to the cell and adsorbed at 0.1 V *vs.* RHE for 5 min. The excess CO was eliminated by passing Ar gas during 25 min and the adsorbed CO was oxidized at a scan rate of 5 mV s^{-1}. A Pt/C commercial catalyst (E-TEK) was used as reference sample. Solutions were prepared from analytical grade H_2SO_4 (Sigma Aldrich), analytical grade ethanol (J. T. Baker) and ultra-pure water (MilliQ, Millipore).

In situ infrared reflection absorption spectroscopy (IRRAS) measurements were carried out by using a MB-100 FT-IR spectrometer (Bomem) equipped with a MCT detector cooled with liquid nitrogen.

Direct ethanol fuel cell (DEFC) tests were carried out using an Autolab PGSTAT 30 connected to a personal computer and using the Autolab software v. 4.9. The cell polarization data were collected at 90 °C/3 atm O_2 pressure by circulating a 1 mol L^{-1} aqueous ethanol solution at the anode. Anode: 1 mg Pt cm^{-2}, cathode: 30% Pt/C, 1 mg Pt cm^{-2}.

3. Results and discussion

3.1. Structural characterization of the Pt–Sn–Ce/C catalysts

The EDX compositions of the carbon supported Pt–Sn–Ce, Pt–Sn/C and Pt–Ce electro-catalysts are reported in Table 1: the average compositions were in agreement with the nominal compositions. The XRD patterns of the Pt–Sn–Ce/C and Pt–Sn/C electrocatalysts and of the commercial Pt/C electrocatalyst by E-TEK are shown in Fig. 1. The first broad peak located at the 2θ value of about 25° is attributed to the (0 0 2) phase of the hexagonal

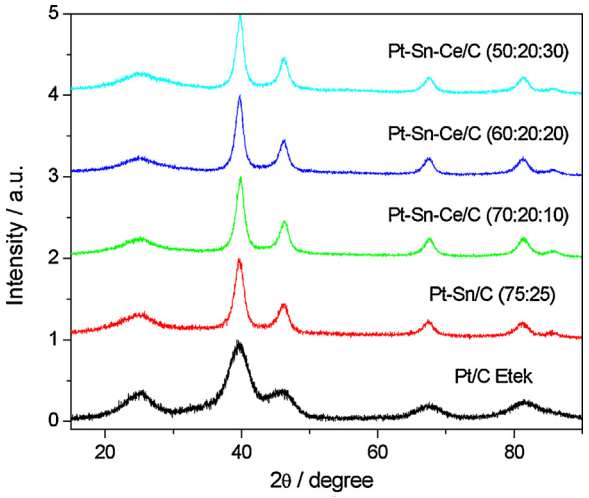

Fig. 1. XRD patterns of the Pt–Sn–Ce/C and Pt–Sn/C electrocatalysts and of the commercial Pt/C electrocatalyst.

Table 1
EDX composition of Pt–Sn–Ce/C, Pt–Sn/C and Pt–Ce/C catalysts.

Catalyst	Pt/at%	Sn/at%	Ce/at%	Sn/Pt	Ce/Pt	(Sn + Ce)/at%
Pt–Sn–Ce/C (70:20:10)	75.0	13.5	11.5	0.18	0.15	25.0
Pt–Sn–Ce/C (60:20:20)	61.0	14.0	25.0	0.23	0.41	39.0
Pt–Sn–Ce/C (50:20:30)	56.5	11.0	32.5	0.19	0.58	43.5
Pt–Sn/C (75:25)	75.0	25.0		0.33		
Pt–Ce/C (90:10)	85.5		14.5		0.17	
Pt–Ce/C (70:30)	65.0		35.0		0.54	
Pt–Ce/C (50:50)	53.0		47.0		0.89	

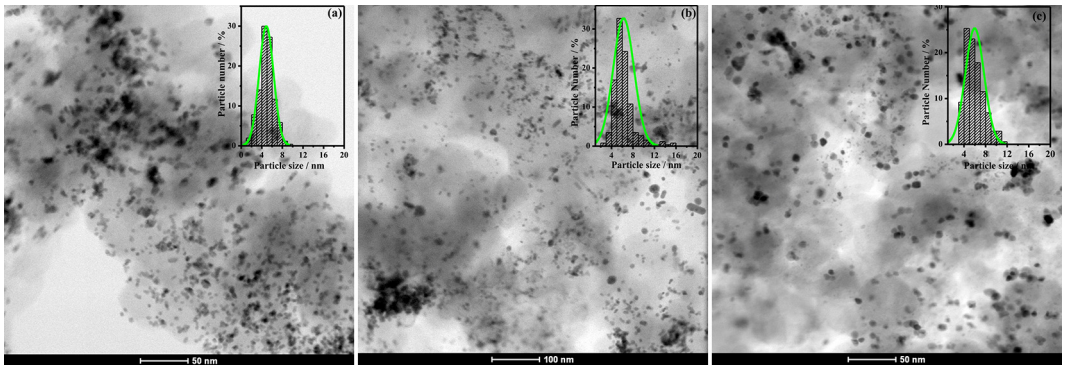

Fig. 2. TEM images and histograms of particle size distribution of Pt–Sn–Ce/C catalysts. (a) Pt–Sn–Ce/C (70:20:10); (b) Pt–Sn–Ce/C (60:20:20); (c) Pt–Sn–Ce/C (50:20:30).

structure of carbon support. The other five diffraction peaks are ascribed to the diffractions of Pt (1 1 1), Pt (2 0 0), Pt (2 2 0), Pt (3 1 1) and Pt (2 2 2) planes, respectively, which represent the characteristics of face centered cubic (fcc) structure of platinum. Only the reflexions of carbon and fcc platinum were present in the patterns of Pt–Sn–Ce/C and Pt–Sn/C catalysts. No substantial shift of these diffraction peaks was observed, which is indicative of no Pt–Sn or Pt–Ce alloy formation. No reflexions of metallic Sn and Ce or Sn and Ce oxides were detected, but their presence cannot be discarded because they may be present in a little amount, in a small particle size or in an amorphous form. Moreover, at the same amount in the catalyst, the reflexions of CeO_x oxides present a lower intensity than Pt, so it is difficult to detect them.

The lattice parameters of Pt/C, Pt–Sn/C and Pt–Sn–Ce/C catalysts are reported in Table 2. The lattice parameters of the Pt–Sn–Ce/C catalysts were in the range 0.3919–0.3925 nm, near to that of Pt/C (0.3921 nm). The fcc Pt peaks in Pt–Sn–Ce/C and Pt–Sn/C electrocatalysts were sharper than those in Pt/C E-TEK, indicating that the crystallite size of Pt in ternary catalysts is larger than that of the commercial platinum. The average crystallite sizes of the Pt nanoparticles were estimated by using Sherrer's equation and are reported in Table 2.

Fig. 2a–c shows the results of TEM analysis of the Pt–Sn–Ce/C catalysts. As can be seen in Fig. 2, Pt particles are homogeneously distributed on the carbon support. The histogram of the particle size distribution reflects quantitatively the size distribution in the Pt–Sn–Ce/C catalysts. The Pt particle size distributions were in the ranges 1.3–9.7 nm, 2.8–15.8 nm and 3.2–11.1 nm for Pt–Sn–Ce (70:20:10), (60:20:20) and (50:20:30), respectively. The average Pt particle size, obtained by the Gaussian curve related to the histograms in Fig. 2, are reported in Table 2. As can be seen in Table 2, the volume averaged particle size of Pt–Sn–Ce/C catalysts obtained from the TEM images were in agreement with the crystallite size calculated from the XRD measurements.

The chemical oxidation states and surface compositions of Pt, Sn and Ce in the Pt–Sn–Ce/C catalysts were determined by XPS analysis. Fig. 3 shows the XPS spectra of the Pt 4*f*, Sn 3*d* and Ce 3*d* regions for each Pt–Sn–Ce/C catalyst and Table 3 lists the assignments

Table 2
Lattice parameter and crystallite size by XRD, and particle size by TEM of Pt–Sn–Ce/C and Pt–Sn/C catalysts and Pt/C by ETEK.

Catalyst	Lattice parameter/nm	Crystallite size (XRD)/nm	Particle size (TEM)/nm
Pt–Sn–Ce/C (70:20:10)	0.3919	5.3	4.9
Pt–Sn–Ce/C (60:20:20)	0.3925	5.5	6.2
Pt–Sn–Ce/C (50:20:30)	0.3925	5.5	6.2
Pt–Sn/C (75:25)	0.3929	4.6	4.1
Pt/C ETEK	0.3921	2.3	

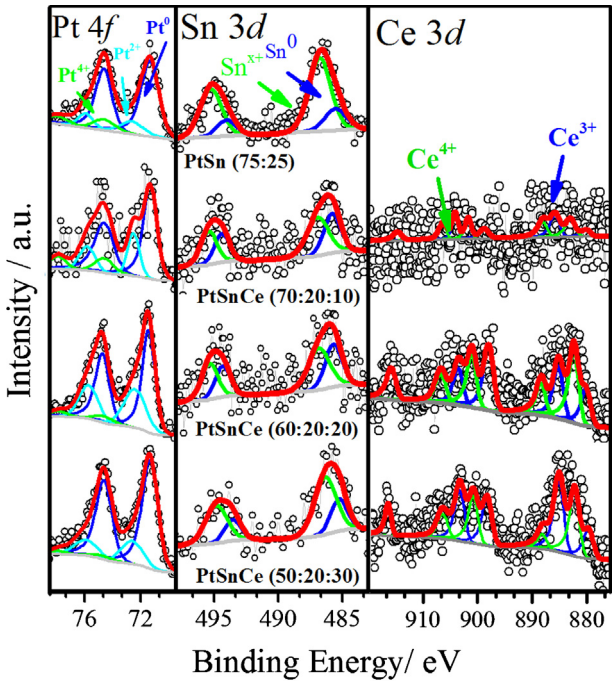

Fig. 3. Pt 4*f*, Sn 3*d* and Ce 3*d* XPS patterns of the Pt–Sn–Ce/C and Pt–Sn/C electrocatalysts.

Table 3
Binding energy values of Pt–Sn–Ce/C and Pt–Sn/C catalysts, with the relative % of different oxidation states indicated in parenthesis and the XPS atomic compositions.

Catalyst	Binding energy (eV)							
	Pt(0) $4f_{7/2}$	Pt(II) $4f_{7/2}$	Pt(IV) $4f_{7/2}$	Sn(0) $3d_{5/2}$	Sn(II,IV) $3d_{5/2}$	Ce(III) $3d_{5/2}$	Ce(IV) $3d_{5/2}$	XPS ratio (at%)
Pt–Sn–Ce/C (70:20:10)	71.3 (65)	72.5 (23)	74.6 (12)	485.8 (39)	486.8 (61)	885.8; 880.1 (47)	883.1; 888.0; 914.4 (53)	85:12:3
Pt–Sn–Ce/C (60:20:20)	71.4 (61)	72.4 (34)	74.6 (5)	484.8 (25)	486.0 (75)	885.3; 880.3 (46)	882.6; 888.5; 915.7 (54)	58:22:20
Pt–Sn–Ce/C (50:20:30)	71.3 (77)	72.6 (20)	74.6 (5)	485.1 (27)	486.3 (73)	885.1; 879.7 (54)	882.3, 888.2; 916.4 (46)	55:12:33
Pt–Sn/C (75:25)	71.3 (74)	71.6 (14)	74.6 (12)	485.1 (25)	486.8 (75)			82:18

of the deconvoluted spectra to various oxidation states and their relative percentages. The Pt 4*f* XPS signals consists of two peaks corresponding to the $4f_{5/2}$ and $4f_{7/2}$ states and each peak can be deconvoluted into three different Pt oxidation states of Pt(0), Pt(II), and Pt(IV). The binding energies (BEs) of the three components of the Pt $4f_{7/2}$ state were *ca.* 71.3, 72.5 and 74.6 eV. The Pt $4f_{7/2}$ signal at 71.3 eV was assigned to zero-valent platinum. The signal at 72.5 eV was attributed to PtO and the signal at 74.6 eV was ascribed to PtO_2. The Sn 3*d* spectrum of Pt–Sn–Ce/C can be deconvoluted in two components, one for Sn(0) and the second for Sn(II/IV). The lower binding energy peak is due to Sn(0) while the higher binding energy peak can be attributed to oxidized species such as Sn(II) or Sn(IV). Distinction between Sn(II) and Sn(IV) is difficult owing to a small difference in the binding energies. As shown in Table 3, as in the case of the Pt–Sn/C catalyst, the most part of Sn on the surface of all the Pt–Sn–Ce/C catalysts was in the oxide form, but a not negligible part (25–40%) was in the Sn(0) form. Considering the amount of Pt(0) and Sn(0), the formation of a Pt-rich PtSn alloy on the catalyst surface cannot be discarded, while the bulk is essentially formed by non alloyed Pt and SnO_x. The absence of an appreciable BE shift of the Pt $4f_{7/2}$ signal related to Pt(0) should be due to the low amount of Sn alloyed. The XPS Ce 3*d* spectrum of CeO_x is rather complex. The peaks in the energy interval between approximately 877 and 903 eV belong to the Ce $3d_{5/2}$ level. There are three peaks (situated at 882–883, 888–890, and 898–899 eV) that may be attributed to the cerium (IV) oxidation state, whereas the other two peaks (situated at 881–882 and 885–886 eV) may be attributed to the cerium (III) state [26]. The peaks from the different oxidation states overlap, making analysis of the structure extremely complicated. The Ce 3*d* spectrum of Pt–Sn–Ce/C was tentatively deconvoluted in three components, one for Ce(III) and the other for Ce(IV). The amount of CeO_2 was *ca.* 60% and that of Ce_2O_3 *ca.* 40%. The surface composition obtained by XPS measurements is reported in Table 3 and the dependence of XPS composition on EDX composition is shown in Fig. 4. As can be seen in Fig. 4, the data match the line with slope = 1, indicating no surface segregation. Some differences between XPS and EDX compositions, however, are present, so, in the following part of this work we have used the XPS composition.

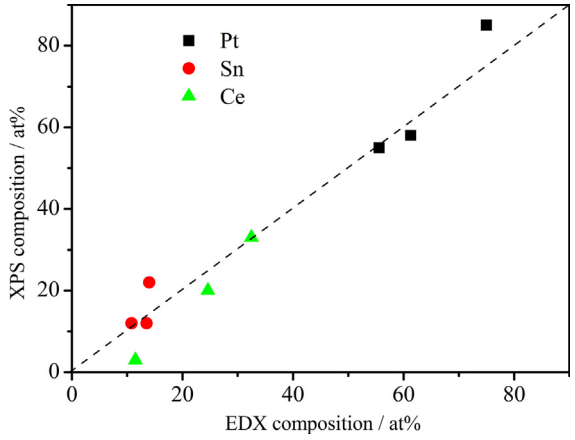

Fig. 4. Dependence of XPS composition on EDX composition of Pt–Sn–Ce/C catalysts.

3.2. Electrochemical characterization of Pt–Sn–Ce/C catalysts

3.2.1. Electrochemical activity of Pt–Sn–Ce/C and Pt–Ce/C catalysts for CO oxidation

The CO stripping profiles of Pt–Ce/C and Pt–Sn–Ce/C catalysts are shown in Fig. 5a and b, respectively. To obtain a better comparison between the catalysts, in Fig. 5 the baseline was subtracted to the first cycle. The CO stripping profiles of Pt–Sn/C has been also reported for comparison. As can be seen in Fig. 5a, all Pt–Ce/C peaks of CO oxidation were sharp and the onset potential was shifted to lower potentials (in the range 0.58–0.71 V *vs.* RHE) with respect to Pt/C (*ca.* 0.8 V *vs.* RHE [10]). Thus, it appears that CeO_2 has the ability to promote the electro-oxidation of adsorbed CO, in agreement with literature data [27–29]. The onset potential for CO oxidation

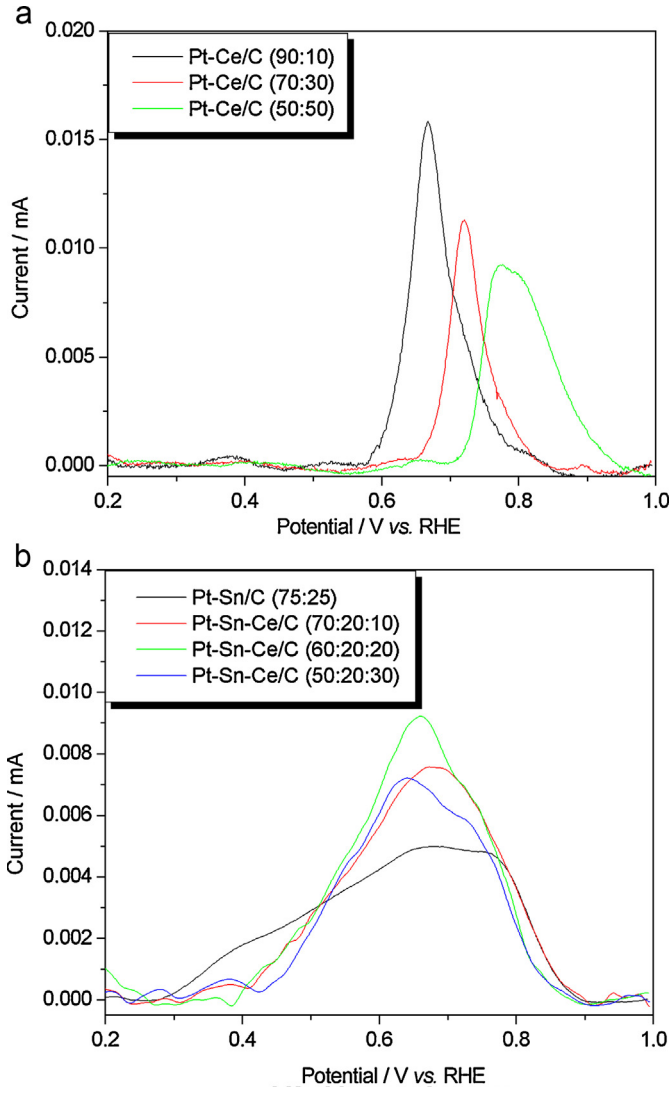

Fig. 5. CO stripping of Pt-Ce/C (a) and Pt-Sn-Ce/C (b) catalysts.

Table 4
$ECSA_{CO}$, current density at 0.4 V ($j_{LSV}^{0.4}$) and 0.6 V ($j_{LSV}^{0.6}$) by LSV, mass specific activity (MSA) at 0.7 V, steady state current density by CA (j_{ss}) and ($j_{ss}^{0.6}/j_{LSV}^{0.6}$) current density ratio for Pt–Sn–Ce/C, Pt–Sn/C, Pt–Ce/C and Pt/C catalysts.

Catalyst	$ECSA_{CO}$ ($m^2\ g_{Pt}^{-1}$)	$j_{LSV}^{0.4}$ ($\mu A\ cm^{-2}$)	$j_{LSV}^{0.6}$ ($\mu A\ cm^{-2}$)	$MSA^{0.7}$ ($mA\ \mu g_{Pt}^{-1}$)	$j_{ss}^{0.6}$ ($\mu A\ cm^{-2}$)	$j_{ss}^{0.6}/j_{LSV}^{0.6}$
Pt–Sn–Ce/C (70:20:10)	11	105	340	0.05	197	0.58
Pt–Sn–Ce/C (60:20:20)	14	357	1458	0.16	493	0.35
Pt–Sn–Ce/C (50:20:30)	14	181	1900	0.38	1023	0.55
Pt–Sn/C (75:25)	10	285	754	0.15	523	0.68
Pt–Ce/C (90:10)	7	6	80	0.02	9	0.11
Pt–Ce/C (70:30)	4	9	81	0.01	21	0.26
Pt–Ce/C (50:50)	10	13	79	0.03	17	0.22
Pt/C ETEK	62	2	50	0.14	65	1.30

moved to higher values with increasing the content of cerium. The onset potential for CO oxidation of the Pt–Sn/C catalyst was close to 0.3 V *vs.* RHE (Fig. 5b), in agreement with previous results regarding CO oxidation on Pt–Sn/C catalysts prepared by the same method [30]. This lower onset potential on the Pt–Sn catalyst was attributed to the presence of oxygenated species on Sn sites formed at lower potentials compared to platinum. Non-alloyed Pt/SnO_2 catalysts showed higher electrocatalytic activity for CO oxidation with lower onset potential compared to Pt/C, although the binding energy of Pt 4*f* showed no change [31]. This result indicated that the Sn(II)/Sn(IV) redox couple should promote the CO oxidation, according to the bifunctional mechanism as:

$$Pt\text{-}CO_{ads} + SnO_2\text{-}OH_{ads} \rightarrow CO_2 + H^+ + e^- \quad (1)$$

The oxidation of adsorbed CO occurred over a large potential range on Pt–Sn in comparison to Pt and Pt–Ce/C, where the adsorbed CO was oxidized in a narrow potential range. The peaks for CO oxidation of the Pt–Sn–Ce/C catalysts were less broad than that of Pt–Sn/C and less sharp than those of Pt–Ce/C catalysts, and the onset potential was nearly independent of the catalyst composition, around 0.43 V *vs.* RHE, an intermediate value between Pt–Sn/C and Pt–Ce/C catalysts, indicating a cooperative effect of Sn and Ce oxides for the CO oxidation. In addition to the effect of SnO_x, also the presence of a PtSn alloy on the catalyst surface should support CO oxidation by both an electronic effect, influencing the CO adsorption, and the bifunctional mechanism [10]. The electrochemically active surface areas (ECSAs) of Pt–Sn–Ce/C, Pt–Sn/C and Pt–Ce/C catalysts were estimated from the CO_{ad} oxidation charge and reported in Table 4. The lower ECSA of Pt–Ce/C than that of ternary catalysts is due to their larges particle size (*ca.* 8 nm).

3.2.2. *Electrochemical activity of Pt–Sn–Ce/C and Pt–Ce/C catalysts for ethanol oxidation*

The electrochemical activity for the ethanol oxidation of Pt–Sn–Ce/C, Pt–Sn/C, Pt–Ce/C and Pt/C catalysts was investigated

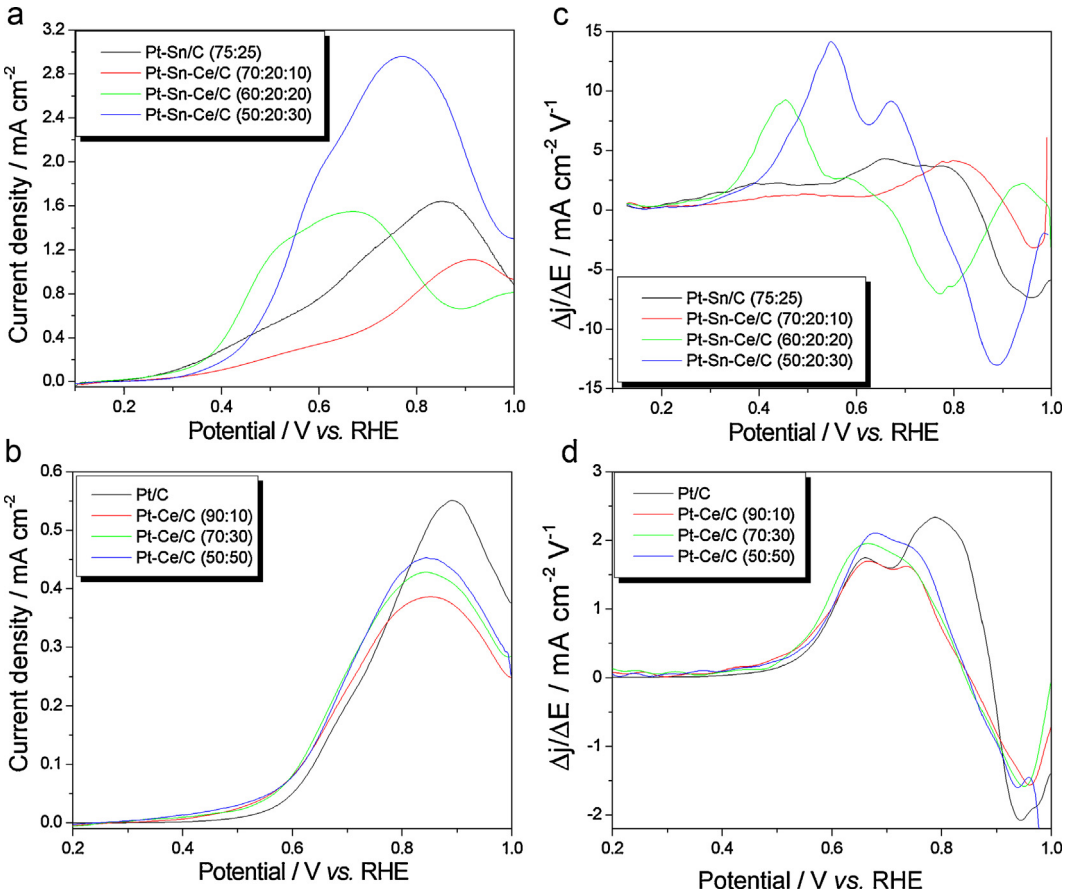

Fig. 6. LSV curve of Pt–Sn–Ce/C and Pt–Sn/C (a), Pt–Ce/C and Pt/C (b), and the derivative of LSV curves ($\partial j_{ECSA}^{LSV}/\partial E$) *vs.* *E* plot of Pt–Sn–Ce/C and Pt–Sn/C (c), Pt–Ce/C and Pt/C (d).

by LSV measurements in H_2SO_4 solution at room temperature and the results are shown in Fig. 6a and b, respectively, with the current density expressed in terms of the ECSA. LSV curves with the current density normalized by the geometric area are poorly significant, as they compare catalysts with both different active surface area and different Pt content. LSV curves with the current density normalized by the ECSA are more interesting, as the current density can be associated to the specific activity of the catalyst. As can be seen in Fig. 6 a, the onset potential for ethanol oxidation of Pt–Sn/C and Pt–Sn–Ce/C (60:20:20) catalysts, that is, the catalysts with a higher Sn content on the surface, was lower than that of Pt–Sn–Ce/C (70:20:10) and (50:20:30) catalysts. On the other hand, the onset potential for ethanol oxidation of all the Pt–Ce/C catalysts was lower than that of Pt/C (Fig. 6b). For fuel cell application, the interesting working potentials of the anode are located between 0.3 and 0.6 V *vs.* RHE to obtain a cell voltage from 0.3 to 0.7 V assuming a potential of about 0.9–1.0 V *vs.* RHE for the cathode, with the highest current density. As can be seen in Table 4, among all the catalysts, at 0.4 V *vs.* RHE the Pt–Sn–Ce/C (60:20:20) catalyst showed the highest current density, while at 0.6 V *vs.* RHE the EOR activity increased with increasing Ce content in Sn-containing catalyst. Clearly, as only a slight positive effect of Ce on the EOR activity of Pt–Ce/C was found both at 0.4 and 0.6 V *vs.* RHE (Table 4), the presence of Sn in Pt–Sn–Ce/C catalysts is essential to attain a high EOR activity. The dependence of the current density at 0.4 V *vs.* RHE from LSV measurements ($j_{LSV}^{0.4}$) on Sn/Pt and (Sn + Ce)/Pt surface atomic ratios is shown in Fig. 7a. The $j_{LSV}^{0.4}$ values of the Pt–Sn–Ce catalysts linearly increased with increasing Sn/Pt, indicating a strong dependence of the current density at 0.4 V *vs.* RHE on Sn content in the catalyst surface, in agreement with the results of Colmati et al. [30], which observed that the current density at 0.4 V *vs.* RHE of Pt–Sn/C catalysts prepared by the formic acid method increases with increasing the amount of non alloyed Sn. On the other hand, $j_{LSV}^{0.4}$ *vs.* (Sn + Ce)/Pt were scattered, indicating the EOR activity at 0.4 V *vs.* RHE is independent of Ce presence. The dependence of the current density at 0.6 V *vs.* RHE from LSV measurements ($j_{LSV}^{0.6}$) on Sn/Pt and (Sn + Ce)/Pt surface atomic ratios is shown in Fig. 7b. In this case, an opposite result was observed that is, the $j_{LSV}^{0.6}$ values of the Pt–Sn–Ce catalysts *vs.* the Sn/Pt ratio were scattered, whereas $j_{LSV}^{0.6}$ almost linearly increased with increasing the (Sn + Ce)/Pt ratio, indicating a strong dependence of the current density at 0.6 V *vs.* RHE on both Sn and Ce content in the catalyst surface.

In the histogram in Fig. 8, we compared the specific activity at 0.4 and 0.6 V *vs*. RHE of Pt–Sn–Ce/C catalysts: (1) with the same Sn surface content but different Ce/Sn surface atomic ratio (Pt–Sn–Ce (70:20:10) and (50:20:30)) and (2) with similar (Sn + Ce) surface content but different Sn/Ce surface atomic ratio (Pt–Sn–Ce/C (60:20:20) and (50:20:30)). As can be seen in Fig. 8, while at 0.4 V *vs.* RHE the increase of Ce content has a slight positive (at fixed Sn) or negative (at similar (Sn + Ce) content) effect on the EOR current density of Pt–Sn–Ce/C catalysts, at 0.6 V *vs.* RHE a considerable improvement in the EOR activity of ternary catalysts with increasing Ce content was observed. Conversely, at 0.6 V *vs.* RHE only a slight positive effect of Ce on the EOR activity of Pt–Ce/C was observed (Table 4). Thus, a synergic effect of Sn and Ce on the EOR activity at 0.6 V *vs.* RHE has to be assumed.

Derivative voltammetry (DV) can help to explain this result. DV represents the rate of change of voltammetric current i with respect to electrode potential E ($\partial j_{ECSA}^{LSV}/\partial E$) and has more voltammetric features than conventional voltammogram [32]. Closely placed voltammetric peaks or shoulders can be resolved in derivative voltammograms, distinguishing ethanol oxidation peaks due to parallel path mechanisms peak in the forward scan. DVs of Pt–Sn–Ce/C and Pt–Ce/C catalysts obtained from the LSV curves reported in Fig. 6a and b are shown in Fig. 6c and d, respectively. DVs of Pt–Sn–Ce/C, Pt–Sn/C, Pt–Ce/C and Pt/C present multiple whereas the corresponding conventional voltammograms show only one peak with weak shoulders at the positive slopes. Ethanol oxidation on Pt, Pt–Ru and Pt–Sn occurs through parallel reaction pathways,

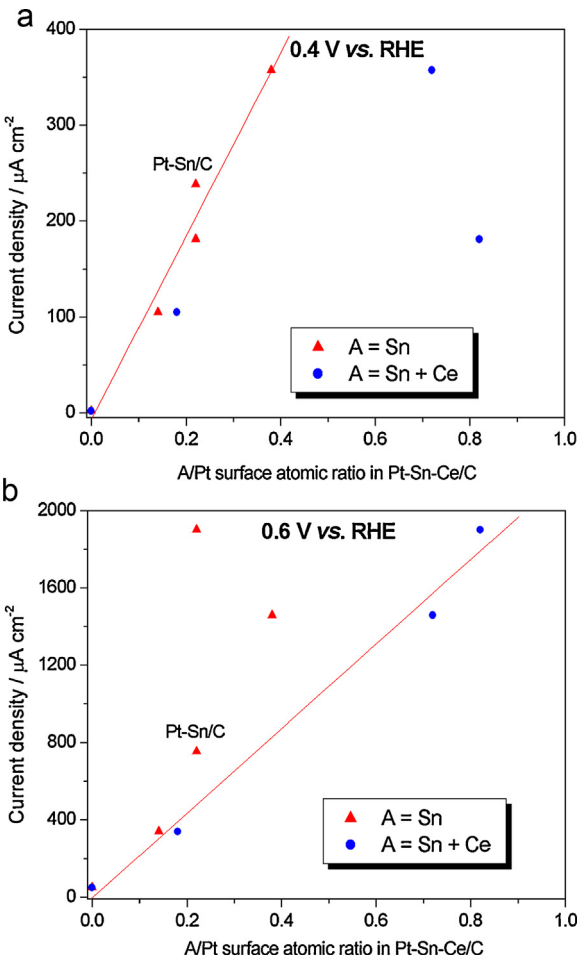

Fig. 7. Dependence of the current density at 0.4 V *vs.* RHE ($j_{LSV}^{0.4}$) (a) and 0.6 V *vs.* RHE ($j_{LSV}^{0.6}$) (b) on surface Sn/Pt and (Sn + Ce)/Pt atomic ratios.

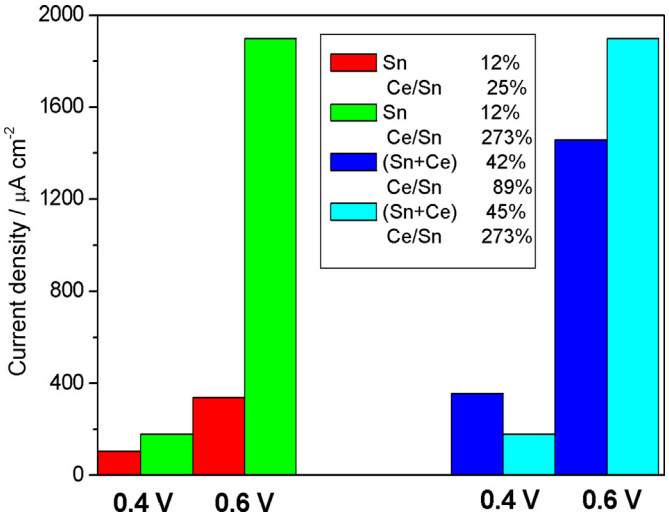

Fig. 8. Histogram of the specific activity at 0.4 and 0.6 V *vs.* RHE of Pt–Sn–Ce/C catalysts with the same Sn surface content but different Ce/Sn surface atomic ratio (Pt–Sn–Ce (70:20:10) and (50:20:30)) and with similar (Sn + Ce) surface content but different Sn/Ce surface atomic ratio (Pt–Sn–Ce/C (60:20:20) and (50:20:30)).

related to intermediate species oxidation, depending on the potential and the metal added to Pt [33–35].

As in the case of Sn and Ru, also Ce does not improve C—C bond cleavage of Pt [36], thus the main products of ethanol oxidation are acetaldehyde (AAL) and acetic acid (AA). AA behaves like a final product, while AAL can be a final products as well as an intermediate to be converted into AA, even in the presence of enhanced reaction activity due to Ce or Sn presence. It is known that the formation of AA and AAL takes place by different pathways [37–39]. For example, ethanol can be adsorbed dissociatively at platinum sites, either via an O-adsorption or a C-adsorption process, to form AAL species [37]. These parallel processes of ethanol adsorption/AAL deadsorption occur at different potentials. As soon as AAL is formed, it can adsorb on platinum sites leading to a Pt-CH_3-CO species:

$$Pt + CHO\text{-}CH_3 \rightarrow Pt\text{-}(CO\text{-}CH_3)_{ads} + H^+ + e^- \quad (2)$$

then, in the presence of a second metal M, such as Sn or Ce, because M is known to activate water at lower potentials than platinum, some OH species can be formed at low potentials on M sites according to reaction:

$$MO_x + H_2O \rightarrow MO_x\text{-}(OH)_{ads} + e^- + H^+ \quad (3)$$

and adsorbed acetaldehyde species can react with adsorbed OH species to produce acetic acid according to:

$$Pt\text{-}(CO\text{-}CH_3)_{ads} + MO_x\text{-}(OH)_{ads} \rightarrow Pt + MO_x + CH_3\text{-}COOH \quad (4)$$

As can be observed in Fig. 6d, two main positive peaks are present in the derivative voltammograms of ethanol oxidation on Pt–Ce and Pt catalysts, that is, a peak at higher potentials (named peak 1) at *ca.* 0.74 V *vs.* RHE for the Ce containing catalysts and at 0.79 V *vs.* RHE for Pt/C, and a peak at lower potentials in the range 0.66–0.68 V (named peak 2), both related to AA + AAL formation by different pathways, labelled as pathway 1 and pathway 2, respectively. The shift to lower potentials of peak 1 maximum of Pt–Ce/C catalysts with respect to Pt/C is similar to the shift of peak 1 maximum observed in Pt–Pr/C catalysts [40], and can be ascribed to an electronic effect, related to Ce_2O_3 presence. Being the anode potential for fuel cell application lower than 0.6 V *vs.* RHE, the pathway 2 is the most interesting. While the peak 2 to peak 1 intensity ratio of Pt/C is <1, this peak intensity ratio of all Pt–Ce/C catalysts was >1, indicating the positive effect of CeO_2 on ethanol oxidation through pathway 2. As can be observed in Fig. 6c, two main positive peaks are also present in the derivative voltammograms of ethanol oxidation on Pt–Sn–Ce/C and Pt–Sn/C catalysts. However, differences in the peak position are present in the DV of these catalysts. It is interesting to compare the DVs of Pt–Sn–Ce/C (60:20:20) and (50:20:30), that is, the catalyst with the highest Sn content with the catalysts with the highest Ce content. The DV of each catalyst presented a peak, which was not observed in the DVs of Pt–Ce/C and Pt/C. The Pt–Sn–Ce/C (60:20:20) shows a large peak centered at *ca.* 0.45 V *vs.* RHE, not too far from the peak for Pt–Sn/C (0.40 V *vs.* RHE), likely related to a reaction pathway involving only Sn, whereas the Pt–Sn–Ce/C (50:20:30) presents a main peak centered at *ca.* 0.55 V *vs.* RHE, likely related to a reaction pathway involving both Sn and Ce. Thus, the high EOR activity of the Pt–Sn–Ce/C (50:20:30) catalyst was not merely due to the sum of the reaction pathway involving Sn (at *ca.* 0.40 V *vs.* RHE) and the reaction pathway involving Ce (at *ca.* 0.67 V *vs.* RHE), but to another reaction pathway (at *ca.* 0.55 V *vs.* RHE), involving both Sn and Ce oxides. At *ca.* 0.55 V *vs.* RHE, a synergic effect of Sn and Ce oxides on ethanol oxidation has to be inferred. The DV results confirm the LSV results, that is, a dependence of the specific activity on potential and on catalyst composition.

IRRAS measurements, reported in Fig. S1 in supplementary data, indicated the presence of AAL (band located around 933 cm^{-1}) and AA (band at ca. 1280 cm^{-1}) in the final products of all the catalysts,

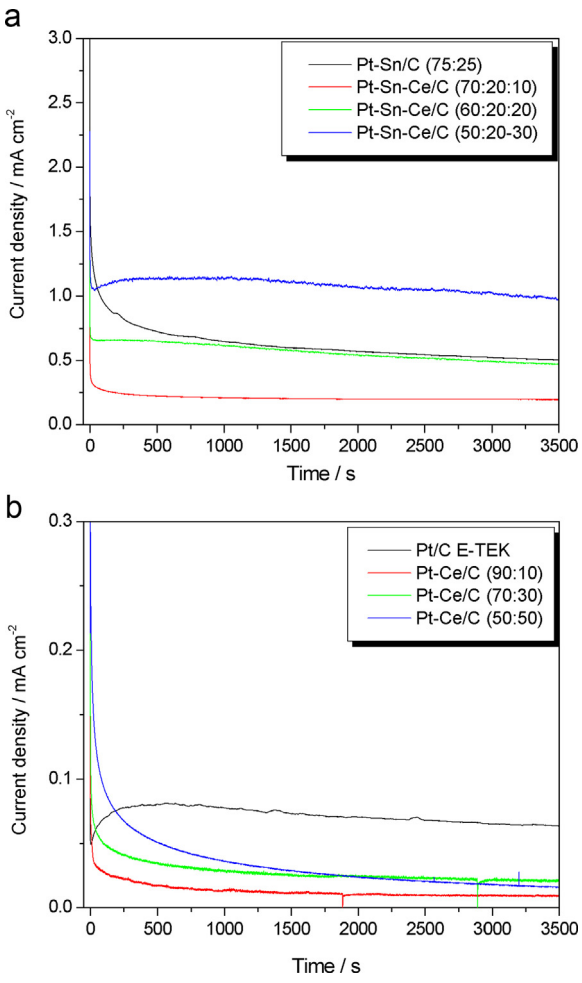

Fig. 9. Current–time curves at 0.6 V *vs.* RHE for Pt–Sn–Ce/C and Pt–Sn/C (a), Pt–Ce/C and Pt/C (b) electrocatalysts.

except AA in the final products of Pt–Ce/C (70:30). CO_2 formation was not detected, but its formation in small amount cannot be discarded. For the Pt–Sn/C and Pt–Sn–Ce/C (60:20:20) catalysts, that is, the catalysts with the highest Sn/Pt surface atomic ratio, the formation of both AAL and AA starts from 0.5 V vs. RHE. For the Pt–Sn–Ce/C (70:20:10) and (50:20:30) catalysts AAL formation starts at a slightly lower potentials (0.4–0.45 V vs. RHE) whereas AA formation at slightly higher potentials (0.55–0.65 V vs. RHE) than Pt–Sn/C and Pt–Sn–Ce/C (60:20:20) catalysts. Finally, for the Pt–Ce/C catalyst, AAL formation starts at higher potentials, 0.8 V vs. RHE. These results indicate that the catalysts with a higher Sn/Pt surface atomic ratio are more effective for the oxidation of AAL to AA, but they are less useful for ethanol dissociative adsorption to form AAL than the catalysts with a lower Sn/Pt surface atomic ratio.

Supplementary figure related to this article can be found, in the online version, at http://dx.doi.org/10.1016/j.apcatb.2014.10.012.

3.2.3. *Short term stability of Pt–Sn–Ce/C catalysts*

To evaluate both the electrocatalytic activity of the Pt–Sn–Ce/C, Pt–Sn/C, Pt–Ce/C and Pt/C catalysts in steady state conditions and the poisoning of the active surface, chronoamperometric experiments were carried out at 0.6 V in 0.5 M H_2SO_4 solution containing ethanol for 3600 s. The ECSA normalized current-time curves for Pt–Sn–Ce/C, Pt–Sn/C, Pt–Ce/C and Pt/C catalysts are shown in Fig. 9a and b. Apart Pt/C, in all CA curves the current drops with time elapsing, rapidly at the beginning and then, also following a slight increase in Pt–Sn–Ce/C (50:20:30), becomes

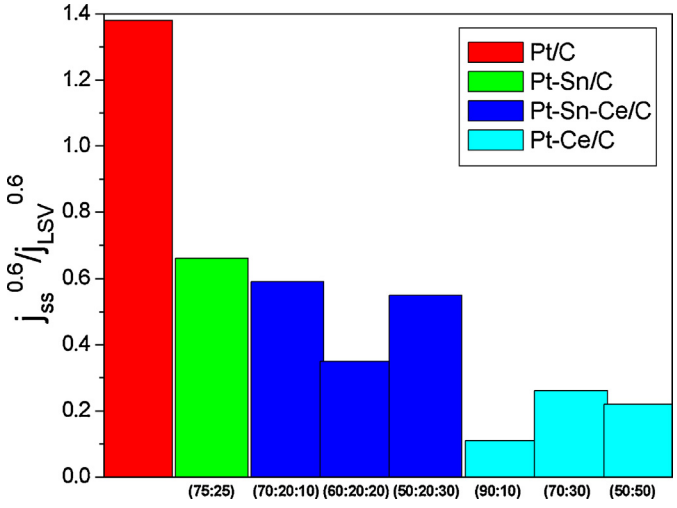

Fig. 10. Histogram of the steady state current density at 0.6 V *vs.* RHE by CA to the current density at 0.6 V *vs.* RHE by LSV ($j_{LSV}^{0.6}$) ratio of Pt–Sn–Ce/C, Pt–Ce/C and Pt/C electrocatalysts.

relatively stable. The decay could be ascribed to poisoning of surface active sites, assuming that initially the active sites are free from adsorbed ethanol molecules, but a new adsorption of ethanol molecules is a function of the liberation of the actives sites by adsorbed intermediate species (CO, CH_x, CH_3CHO and CH_3COOH) formed during the first period of time, which are responsible for poisoning of the catalytic sites. The order of activity at the steady state (after 3500 s, $j_{LSV}^{0.6}$) of Sn-containing catalysts was Pt–Sn–Ce/C (50:20:30) > Pt–Sn/C ≈ Pt–Sn–Ce/C (60:20:20) > Pt–Sn–Ce/C (70:20:10). A way to evaluate the true stability of these catalysts is to compare the steady state current density at 0.6 V *vs.* RHE by CA to the current density at 0.6 V *vs.* RHE by LSV ($j_{LSV}^{0.6}$) ratio. As can be seen in Table 4 and in the histogram in Fig. 10, the poisoning of the Pt–Sn–Ce/C catalysts was considerably higher than that of Pt/C, slightly higher than Pt–Sn/C, but lower than that of Pt–Ce/C catalysts.

3.2.4. Test in direct ethanol fuel cells

DEFC polarisation and power density curves at 90 °C using Pt–Sn/C and Pt–Sn–Ce/C as anode catalysts are shown in Fig. 11. As

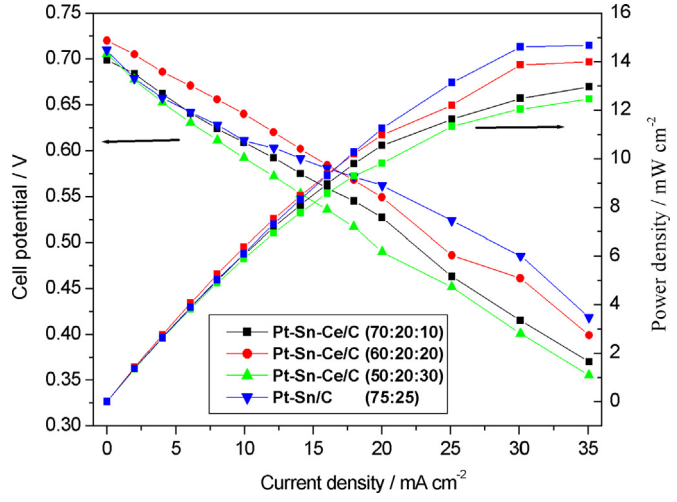

Fig. 11. Polarization and power density curves obtained in a single DEFC with Pt–Sn/C and Pt–Sn–Ce/C as anode electrocatalysts for ethanol oxidation at 90 °C and 3 atm O_2 pressure using a 1 mol L^{-1} ethanol solution. Anode metal loading 1 mg cm^{-2}. Cathode: 30 wt% Pt/C, Pt loading 1 mg cm^{-2}.

can be seen in Fig. 11, the DEFCs with Pt–Sn–Ce/C (60:20:20) and Pt–Sn/C (75:25) as anode catalysts showed the best performance for current densities lower and higher than 15 mA cm^{-2}, respectively. These catalysts presented a higher surface Sn/Pt atomic ratio than that of the Pt–Sn–Ce/C (70:20:10) and Pt–Sn–Ce/C (50:20:30) catalysts, indicating that in DEFC operation at 90 °C a higher Sn content is more effective for ethanol oxidation than the addition of Ce to Pt–Sn/C.

The results of this work were compared with those of De Souza et al. [22]. They investigated the effect of Ce on the EOR activity of partially alloyed Pt–Sn/C catalysts carrying out CA measurements and DEFC tests on Pt–Sn–Ce/C catalysts in three different compositions. As in the present work, among the various Pt–Sn–Ce/C catalysts, only one showed a steady state current density higher than that of the binary Pt–Sn/C. Then, they tested this catalyst in a single DEFC and, unlike our results, observed a higher performance of the cell with Pt–Sn–Ce/C (68:22:10) as anode catalyst than that with Pt–Sn/C. They explained their results by a synergistic effect between ceria and tin sites. In this work, the effect of Ce on the EOR activity of Pt–Sn was analyzed more in detail by LSV and derivative LSV. It was highlighted for the first time that on the Pt–Sn–Ce/C catalysts the EOR takes place trough different pathways, depending on the potential, involving only Sn at *ca.* 0.40 V *vs.* RHE and both Sn and Ce at *ca.* 0.55 V *vs.* RHE. The knowledge of the potential range, at which the different metals are effective for ethanol oxidation, is a useful tool for the design of new multimetal catalysts.

From the current density/potential plots in Fig. 6a and b and the ECSA values in Table 4, we evaluated the mass specific activity (MSA) at 0.7 V *vs.* RHE of PtSnCe, Pt–Sn/C, Pt–Ce/C and Pt/C catalysts. As reported by Brouzgou et al. [41], the MSA at 0.7 V of the most of the examined catalysts belonged to the region between the values 0.1 and 1 mA μg_{Pt}^{-1}. As shown in Table 4, the MSA values of the Pt–Sn–Ce/C (50:20:30) and (60:20:20), Pt–Sn/C and Pt/C catalysts fell in this region, whereas the MSA of the Pt–Sn–Ce/C (70:20:10) and all the Pt–Ce/C was <0.1 mA μg_{Pt}^{-1}. As for the ECSA normalized current density at 0.6 V vs. RHE, the Pt–Sn–Ce/C (50:20:30) catalyst presented the highest MSA value, 0.38 mA μg_{Pt}^{-1}. Considering that the active area of the Pt–Sn–Ce/C (50:20:30) catalyst is *ca.* 25% of that of Pt/C, there is room for an increase of the ECSA of Pt–Sn–Ce/C (50:20:30): The enhancement in the active area should allow this catalyst to achieve a very high MSA value, >1 mA μg_{Pt}^{-1}.

4. Conclusions

Carbon supported Pt–Sn–Ce catalysts were prepared by a modified formic acid method, and their electrocatalytic activity for ethanol oxidation and short-term stability was compared with that of Pt–Sn/C, Pt–Ce/C and Pt/C catalysts. The EOR activity of ternary catalysts was considerably higher than that of Pt–Ce/C and Pt/C, mainly due to Sn presence in the catalysts. The onset potential for ethanol oxidation decreased with increasing Sn content on the catalyst surface. The effect of Ce presence in Pt–Sn–Ce catalysts on the EOR activity was related to the potential: indeed, at 0.4 V *vs.* RHE the effect of Ce on the EOR activity was negligible, while it was remarkable at 0.6 V *vs.* RHE. Derivative voltammetry showed that ethanol electrooxidation on Pt–Sn–Ce/C catalysts takes place by two main pathway at different potentials (0.44 and 0.55 V *vs.* RHE), depending on the Ce/Sn atomic ratio. At similar Sn or (Sn + Ce) content, for Ce/Sn atomic ratios <1 (0.25 or 0.90), the ethanol oxidation takes place preferentially through the pathway at lower potential, involving only Sn, whereas for a Ce/Sn atomic ratio of 2.75, the ethanol oxidation preferentially occurs through the pathway at higher potential, involving both Sn and Ce. Short term stability tests indicated that the Pt–Sn–Ce/C catalysts were considerably less tolerant to the poisoning by ethanol oxidation intermediate

species than Pt/C, slightly less poisoning tolerant than Pt–Sn/C, but more poisoning tolerant than the Pt–Ce/C catalysts. DEFC tests at 90 °C indicated that a higher Sn surface content is more effective for ethanol oxidation than the addition of Ce to Pt–Sn/C.

Acknowledgements

The authors thank the Grants 2011/50727-9 and 2012/12189-8, São Paulo Research Foundation (FAPESP) and thank CNPq (Grant 307623/2012-2). The authors also wish to thank National Synchrotron Light Laboratory, Brazil (LNLS) for assisting with the XPS measurements (Project SXS – 15166).

References

[1] C. Lamy, S. Rousseau, E.M. Belgsir, C. Coutanceau, J.M. Leger, Electrochim. Acta 49 (2004) 3901–3908.
[2] F. Vigier, C. Coutanceau, A. Perrard, E.M. Belgsir, C. Lamy, J. Appl. Electrochem. 34 (2004) 439–446.
[3] F. Vigier, S. Rousseau, C. Coutanceau, J.M. Leger, C. Lamy, Top. Catal. 40 (2006) 111–121.
[4] H. Wang, Z. Jusys, R.J. Behm, J. Power Sources 154 (2006) 351–359.
[5] E. Antolini, J. Power Sources 170 (2007) 1–12.
[6] P.E. Tsiakaras, J. Power Sources 171 (2007) 107–112.
[7] E. Antolini, Appl. Catal. B: Environ. 74 (2007) 324–336.
[8] E. Antolini, Appl. Catal. B: Environ. 74 (2007) 337–350.
[9] J. Friedl, U. Stimming, Electrochim. Acta 101 (2013) 41–58.
[10] E. Antolini, E.R. Gonzalez, Catal. Today 160 (2011) 28–38.
[11] E. Antolini, ChemSusChem 6 (2013) 966–973.
[12] S. Beyhan, C. Coutanceau, J.-M. Léger, T.W. Napporn, F. Kadırgan, Int. J. Hydrogen Energy 38 (2013) 6830–6841.
[13] S. Beyhan, J.-M. Léger, F. Kadırgan, Appl. Catal. B: Environ. 144 (2014) 66–74.
[14] S. Beyhan, J.-M. Léger, F. Kadırgan, Appl. Catal. B: Environ. 130–131 (2013) 305–313.
[15] F. Colmati, E. Antolini, E.R. Gonzalez, J. Alloys Compd. 456 (2008) 264–270.
[16] M. Li, A. Kowal, K. Sasaki, N. Marinkovic, D. Su, E. Korach, P. Liu, R.R. Adzic, Electrochim. Acta 55 (2010) 4331–4338.
[17] E.V. Spinace, R.R. Dias, M. Brandalise, M. Linardi, A.O. Neto, Ionics 16 (2010) 91–95.
[18] W.X. Du, Q. Wang, C.A. LaScala, L.H. Zhang, D. Su, A.I. Frenkel, V.K. Mathur, X.W. Teng, J. Mater. Chem. 21 (2011) 8887–8892.
[19] E. Antolini, J. Perez, Int. J. Hydrogen Energy 36 (2011) 15752–15765.
[20] C.L. Perkins, M.A. Henderson, C.H.F. Peden, G.S. Herman, J. Vac. Sci. Technol. A 19 (2001) 1942–1946.
[21] Q. Tan, C. Du, Y. Sun, L. Du, G. Yin, Y. Gao, J. Power Sources 263 (2014) 310–314.
[22] R.F.B. De Souza, J.C.M. Silva, M.H.M.T. Assumpção, A.O. Neto, M.C. Santos, Electrochim. Acta 117 (2014) 292–298.
[23] E.R. Gonzalez, E.A. Ticianelli, A.L.N. Pinheiro, J. Perez, INPI-SP No. 00321, Brazil, 1997.
[24] J. Gurgul, M.T. Rinke, I. Schellenberg, R. Pottgen, Solid State Sci. 17 (2013) 122–127.
[25] D.R.M. Godoi, J. Perez, H.M. Villullas, J. Power Sources 195 (2010) 3394–3401.
[26] L. Truffault, M.T. Ta, T. Devers, K. Konstantinov, V. Harel, C. Simmonard, C. Andreazza, I.P. Nevirkovets, A. Pineau, O. Verona, J.P. Blondeau, Mater. Res. Bull. 45 (2010) 527–535.
[27] D.J. Guo, Z.H. Jing, J. Power Sources 195 (2010) 3802–3805.
[28] D.M. Gu, Y.Y. Chu, Z.B. Wang, Z.Z. Jiang, G. Yin, Y. Liu, Appl. Catal. B: Environ. 102 (2011) 9–18.
[29] R. Lin, C.H. Cao, H.Y. Zhang, H.B. Huang, J.X. Ma, Int. J. Hydrogen Energy 37 (2012) 4648–4656.
[30] F. Colmati, E. Antolini, E.R. Gonalez, J. Electrochem. Soc. 154 (2007) B39–B47.
[31] T. Okanishi, T. Matsui, T. Takeguchi, R. Kikuchi, K. Eguchi, Appl. Catal. A: Gen. 298 (2006) 181–187.
[32] A. Murthy, A. Manthiram, J. Phys. Chem. C 116 (2012) 3827–3832.
[33] S.C. Chang, L.W.H. Leung, M.J. Weaver, J. Phys. Chem. US 94 (1990) 6013–6021.
[34] H. Hitmi, E.M. Belgsir, J.M. Leger, C. Lamy, R.O. Lezna, Electrochim. Acta 39 (1994) 407–415.
[35] J.P.I. de Souza, S.L. Queiroz, K. Bergamaski, E.R. Gonzalez, F.C. Nart, J. Phys. Chem. B 106 (2002) 9825–9830.
[36] R.F.B. De Souza, L.S. Parreira, J.C.M. Silva, F.C. Simoes, M.L. Calegaro, M.J. Giz, G.A. Camara, A.O. Neto, M.C. Santos, Int. J. Hydrogen Energy 36 (2011) 11519–11527.
[37] S. Rousseau, C. Coutanceau, C. Lamy, J.M. Leger, J. Power Sources 158 (2006) 18–24.
[38] I. Kim, O.H. Han, S.A. Chae, Y. Paik, S.H. Kwon, K.S. Lee, Y.E. Sung, H. Kim, Angew. Chem. Int. Ed. 50 (2011) 2270–2274.
[39] M.H. Shao, R.R. Adzic, Electrochim. Acta 50 (2005) 2415–2422.
[40] P.G. Corradini, E. Antolini, J. Perez, J. Power Sources 251 (2014) 402–410.
[41] A. Brouzgou, S.Q. Song, P. Tsiakaras, Appl. Catal. B: Environ. 127 (2012) 371–388.